RSC Advances

PAPER

Check for updates

Synthesis, structure and optical performance of red-emitting phosphor $Ba_5AlF_{13}:Mn^{4+}$

Lin Qin, Peiqing Cai, Cuili Chen, Jing Wang and Hyo Jin Seo (ID) *

Mn^{4+}-activated cubic phase Ba_5AlF_{13} red phosphors were prepared by the two-step coprecipitation method. The structural and optical features were characterized on the basis of X-ray diffraction (XRD), transmission electron microscopy (TEM), emission and excitation spectra, and luminescence decay curves. The $Ba_5AlF_{13}:Mn^{4+}$ phosphors can be efficiently excited by near-UV to blue light and exhibit bright red emission at around 627 nm, which is assigned to the $^2E_g \rightarrow {}^4A_{2g}$ transition of the $3d^3$ electrons in $[MnF_6]$ octahedra. Temperature dependent emission spectra and decay curves from 10 to 550 K were measured to deeply understand the luminescence mechanism of Mn^{4+} in the Ba_5AlF_{13} lattice. Notably, this novel red phosphor shows excellent anti-thermal quenching behaviour ($\sim$700% of emission intensity at 300 K relative to 10 K).

1. Introduction

Compared with traditional oxide lattices, fluoride lattices have rich advantages; for example, lower phonon energy, high refractive index, high quantum efficiency, and high thermal stability.[1] From the viewpoint of the low quenching probability of the excited states of the dopant ions, many fluoride lattices have been chosen as phosphors with various activators. Mn^{4+}, as a transition metal ion with an unfilled $3d^3$ electron shell, plays an important role in lighting and display fields.[2] Contrary to the rare-earth-ions with the parity-forbidden f–f transition, the luminescence properties of Mn^{4+} with the d–d transition are easily influenced by various factors of the coordination environment. In fluoride lattices, Mn^{4+} prefers to occupy sites with octahedral coordination, on which a strong crystal field acts. Therefore, the Mn^{4+} ions exhibit an intense broad absorption band in the wavelength region near UV (550 nm) and a series of sharp emission lines peaking at around 630 nm.[3,4] Due to these characteristics, considerable attention has been focused on this field.

A series of Mn^{4+} activated red phosphors with high luminous efficacy have been reported as candidates for red-emitting phosphors, especially, Mn^{4+}-doped fluoride hosts. Mn^{4+}-activated microcrystals of K_2TiF_6 were successfully synthesized by Zhu *et al.* in 2014.[5] The K_2TiF_6 microcrystals presented strong line emission with high luminescence quantum yield as high as 98%, high thermal stability, and extremely high emission intensity. Mn^{4+}-doped alkaline hexa-fluorides, $B_2XF_6:Mn^{4+}$ (B = K, Cs, Rb; X = Ti, Si and Ge), are well known as excellent red-

emitting phosphors for warm w-LEDs.[6–8] However, further exploration of novel Mn^{4+}-doped fluorides for red phosphors is deserved, and their properties should be investigated more deeply.

Here, in this work, we choose the Mn^{4+}-doped fluoride Ba_5AlF_{13} as a red-emitting phosphor, which has not yet been reported in the literature to our best knowledge. The $Ba_5AlF_{13}:Mn^{4+}$ nanoparticles were synthesized *via* the two-step coprecipitation method. The phase formation, morphological features, excitation and emission spectra and thermal quenching behaviours were further investigated. The obtained product possesses a red line-emission spectrum with high thermal stability, which has the potential to enhance the color rendering index of an LED device.

2. Experimental

2.1 Synthesis process

The $Ba_5AlF_{13}:Mn^{4+}$ nanoparticles were prepared *via* the two-step coprecipitation method as shown in Fig. 1. The chemical
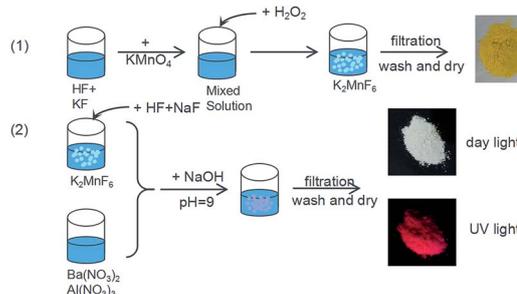

Fig. 1 Two-step synthesis of the $Ba_5AlF_{13}:Mn^{4+}$ nanoparticles.

Department of Physics and Interdisciplinary Program of Biomedical, Mechanical and Electrical Engineering, Pukyong National University, Busan 608-737, Republic of Korea. E-mail: hjseo@pkun.ac.kr

reagents in the synthesis process were $KMnO_4$, KF, HF, $Ba(NO_3)_2$, $Al(NO_3)_3$, NaF, H_2O_2, and NaOH. Firstly, the tetravalent manganese source K_2MnF_6 was synthesized according to Bode's method.[9] The starting materials KF and $KMnO_4$ were both dissolved in HF solution. The mixed solution was stirred for at least 30 min and then doped with H_2O_2 aqueous solution drop by drop until the yellow precipitate K_2MnF_6 was obtained. In the process of preparing the Ba_5AlF_{13}:Mn^{4+} nanoparticles, K_2MnF_6 was added to the HF solution, and then a double molar amount of NaF was added to yield the solution A.

In a separate vessel, $Ba(NO_3)_2$ and $Al(NO_3)_3$ were both dissolved in water to yield solution B. Then, the A and B solutions were mixed together, and an appropriate amount of NaOH was added drop-wise while stirring the solution to adjust the pH value to about 9. Finally, the resulting white slurry was filtered, washed several times using distilled water and then dried at 180 °C for 5 h.

2.2 Characterization

The structure of the Ba_5AlF_{13}:Mn^{4+} nanoparticles was examined by XRD on a Rigaku D/Max 2000 diffractometer with operating parameters set to 40 kV and 30 mA. Transmission electron microscopy (TEM) was conducted to investigate the surface morphology of the samples. The samples were excited by using a 488 nm argon-ion laser and 355 nm pulsed Nd-YAG laser. The luminescence signal was detected using a photomultiplier tube (PMT, Hamamatsu, R928, Shizuoka, Japan) mounted on a 75 cm monochromator (Acton Research Corp. Pro-750). A 450 W Xe lamp dispersed by a 25 cm monochromator (Acton Research Corp. Pro-250) was used as a light source for the excitation and emission spectra. The time-resolved signal was digitized by means of a 500 MHz Tektronix DPO 3054 scope.

3. Results and discussion

3.1 Structural characterization

Fig. 2 shows the XRD patterns of the Ba_5AlF_{13}:Mn^{4+} nanoparticles as functions of Mn^{4+} concentration. The standard 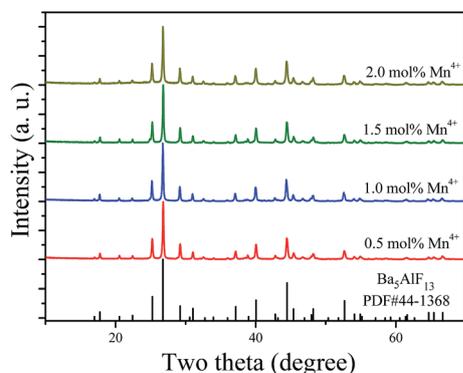PDF card (PDF#44-1368) is displayed for comparison. All the diffraction peaks match well with the standard PDF card, indicating that the Ba_5AlF_{13}:Mn^{4+} nanoparticles with different Mn^{4+} concentrations have been prepared as desired through the two-step coprecipitation method. The Ba_5AlF_{13}:Mn^{4+} nanoparticles crystallize in a cubic space group, $Fd\bar{3}m$. The unit cell parameters are $a = b = c = 17.378$ Å, $\alpha = \beta = \gamma = 90°$, $V = 4427.83$ Å^3 and $Z = 3$.[10] Although Ba_5AlF_{13} and K_2MnF_6 have different crystal structures and there is a mismatch in the valence states between Al^{3+} and Mn^{4+}, the Mn^{4+} ions can also be incorporated into the host lattice of Ba_5AlF_{13} due to the similar ionic radii of Mn^{4+} (coordination number (CN) = 6, 0.53 Å) in $[MnF_6]$ and Al^{3+} (CN = 6, 0.535 Å) in $[AlF_6]$.[11]

Fig. 3 shows the structural map of Ba_5AlF_{13} and an illustration of an $[AlF_6]$ octahedron according to the atomic coordinate data from ref. 10. The Ba_5AlF_{13} lattice contains only one unique crystallographic site of Al^{3+}. All the Al^{3+} ions are located at the center of the regular octahedron $[AlF_6]$, while Ba^{2+} forms $[Ba_{(2)}F_8]$ and $[Ba_{(1)}F_{10}]$ polyhedra connected together with the $[AlF_6]$ octahedra. Since the ionic radius (0.530 Å) of Mn^{4+} is a little smaller than that (0.535 Å) of Al^{3+}, the Mn^{4+}–F^- distance is probably smaller than the Al^{3+}–F^- distance. This means that a distorted system of $[MnF_6]$ octahedra is preserved.

The actual size and morphology of the particles were analysed by TEM. Fig. 4a is a typical TEM image of the Ba_5AlF_{13}:Mn^{4+} nanoparticles. The size of the nanoparticles is estimated to be about 120×120 nm^2. Fig. 4b shows the high-resolution TEM (HRTEM) image confirming the single-crystalline nature of the Ba_5AlF_{13}:Mn^{4+} nanoparticles. In addition, the selected area electron diffraction (SAED) pattern (the inset of Fig. 4b) exhibits the cubic symmetry ascribed to the Ba_5AlF_{13}:Mn^{4+} nanoparticles. The spacing of 3.33 Å corresponds to the (333) reflections of the Ba_5AlF_{13}:Mn^{4+} nanoparticles.

3.2 Spectroscopic properties of Mn^{4+} ions in Ba_5AlF_{13} lattice

The energy level scheme of Mn^{4+} in the lattice can be described by using the Tanabe–Sugano diagram and configuration coordinate model as shown in Fig. 5a and b, respectively. The
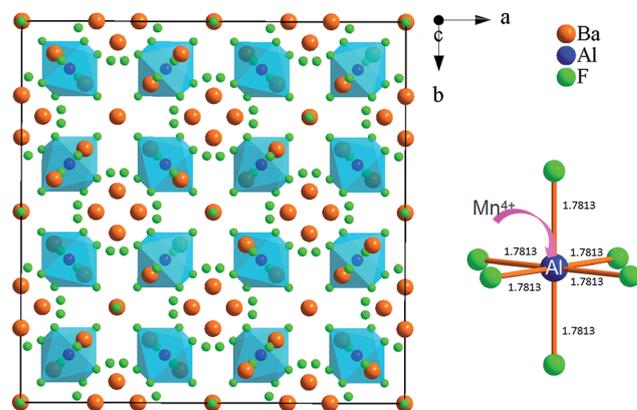

Fig. 2 X-ray diffraction patterns of Ba_5AlF_{13}:Mn^{4+} nanoparticles as functions of Mn^{4+} concentration. The PDF card is displayed for comparison.

Fig. 3 Unit cell of the cubic-type $Fm\bar{3}m$ crystal structure of Ba_5AlF_{13} projected along the c axis and coordination of the Al^{3+}/Mn^{4+} ions in this cubic-type crystal structure. Ba, F, and Al/Mn ions are represented with orange, green, and blue spheres, respectively.
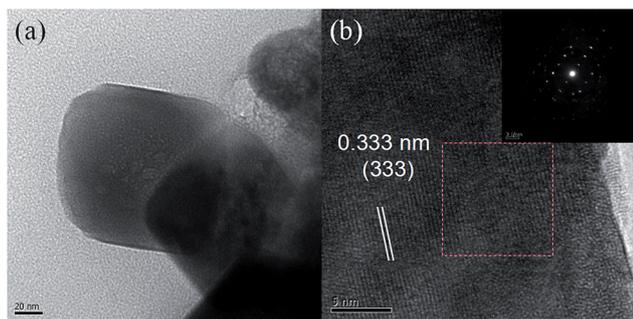
Fig. 4 Typical TEM image (a), HRTEM image (b), and the selected area electron diffraction pattern (the inset of b) of Ba_5AlF_{13}:Mn^{4+} nanoparticles.

luminescence characteristics of the Mn^{4+} ions depend highly on the crystal field strength except for the $^2T_{1g}$ and ^2E_g states. The excitation spectrum of Mn^{4+} corresponds to the spin allowed $^4A_{2g} \rightarrow {}^4T_{2g}$ and $^4A_{2g} \rightarrow {}^4T_{1g}$ transitions, while the emission spectrum belongs to the spin-forbidden d–d transition from the ^2E_g state to the $^4A_{2g}$ state as in Fig. 5b. The lateral displacement between the parabolas of ground state $^4A_{2g}$ and excited state $^4T_{1g}$ (or $^4T_{2g}$) is large, while there is a small displacement between the parabolas of $^4A_{2g}$ and ^2E_g. A larger displacement implies a stronger electron–phonon interaction giving rise to a larger spectral bandwidth of the transition.[12] Thus, intense excitation bands with relatively large bandwidths are expected for the transitions between these states, as well as sharp emission lines due to the $^2E_g \rightarrow {}^4A_{2g}$ transition of Mn^{4+}.

The room temperature excitation spectrum of Ba_5AlF_{13}:Mn^{4+} (0.5 mol%) is shown in Fig. 5c. The excitation spectrum is composed of two broad bands with the maxima at 360 and 460 nm corresponding to the spin allowed $^4A_{2g} \rightarrow {}^4T_{1g}$ and $^4A_{2g} \rightarrow {}^4T_{2g}$ transitions of Mn^{4+}, respectively. A slight splitting phenomenon can be observed in the excitation band corresponding to the $^4A_2 \rightarrow {}^4T_2$ transition but is not observed for the $^4A_2 \rightarrow {}^4T_1$ transition, probably due to a strong overlap with the re-absorption band of the $^4A_2 \rightarrow {}^2T_1$ and $^4A_2 \rightarrow {}^2E$ transitions.[13] The excitation spectrum indicates that the red phosphor doped with Mn^{4+} can be effectively excited by near UV/blue light, which is especially ideal for blue light excitation LED chips.

Contrary to the excitation spectrum, the emission spectrum belongs to the spin-forbidden d–d transition from the ^2E_g state to the $^4A_{2g}$ state of Mn^{4+}, as shown in Fig. 5d. The emission spectrum consists of several sharp lines with the main peak at 627 nm. In general, the zero-phonon line (ZPL) of Mn^{4+} in fluoride lattices is located at around 620 nm.[3] The three peaks at wavelengths longer than 620 nm belong to Stokes ν_6 (t_{2u} bending), ν_4 (t_{1u} bending), and ν_3 (t_{1u} stretching) modes, whereas the two peaks at wavelengths shorter than 620 nm belong to anti-Stokes ν_6 (t_{2u} bending) and ν_4 (t_{1u} bending) modes. The ZPL is not observable for highly symmetrical lattice environments, for example, Rb_2SiF_6:Mn^{4+} and $BaTiF_6$:Mn^{4+} red phosphors.[6,14] More distorted coordination environments cause a stronger intensity of the ZPL line.[6] The intense ZPL observed in the emission spectrum of the Ba_5AlF_{13}:Mn^{4+} nanoparticles indicates that the
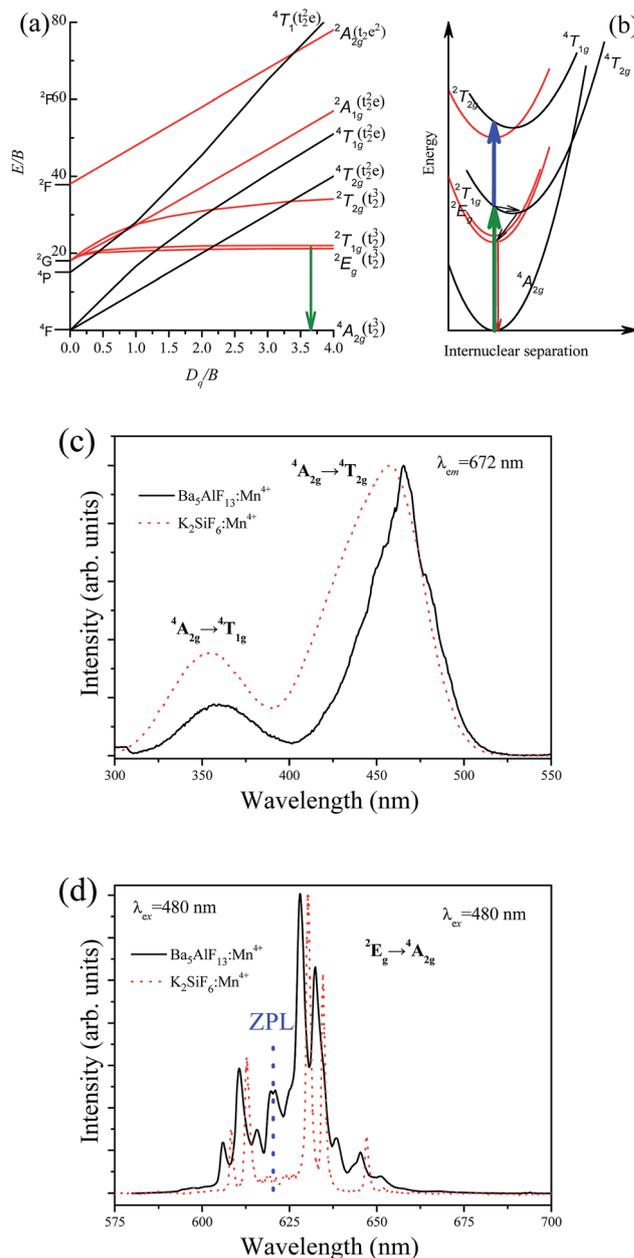

Fig. 5 (a) Tanabe–Sugano energy-level diagram for d^3 ions in the octahedrally coordinated environment. (b) Configurational coordination diagram for Mn^{4+} ions in fluoride hosts. Normalized excitation spectrum (c) and emission spectrum (d) of Ba_5AlF_{13}:Mn^{4+} (0.5 mol%) compared with the well-known K_2SiF_6:1% Mn^{4+} red phosphor.

Mn^{4+} ions experience a lower crystal field symmetry which is mainly due to the distorted $[MnF_6]$ octahedron in the Ba_5-AlF_{13}:Mn^{4+} lattice. According to ref. 6, the existence of ZPL emission in a Mn^{4+} doped phosphor can further improve the color rendering index. The CIE chromaticity coordinates of Ba_5AlF_{13}:Mn^{4+} are calculated to be ($x = 0.691$, $y = 0.31$), which are close to the National Television System Committee (NTSC) standard values for red color ($x = 0.67$, $y = 0.33$).[15]

The local crystal field strength D_q and two Racah parameters B and C can be introduced to describe the unique energy levels

of the Mn^{4+} ions in the Ba_5AlF_{13} lattice.[2] The local crystal field strength D_q is given by the mean peak energy of the $^4A_{2g} \rightarrow {}^4T_{2g}$ transition as obtained by the following equation:

$$D_q = E(^4A_{2g} - {}^4T_{2g})/10 \qquad (1)$$

In this work, $10D_q$ is estimated to be 21 500 cm^{-1} from the excitation spectrum. On the basis of the peak energy difference (11 900 cm^{-1}) between the $^4A_{2g} \rightarrow {}^4T_{2g}$ and $^4A_{2g} \rightarrow {}^4T_{1g}$ transitions, the Racah parameters B and C can be evaluated by the expressions:

$$\frac{D_q}{B} = 15(x-8)/(x^2 - 10x) \qquad (2)$$

$$\frac{E(^2E_g - {}^4A_{2g})}{B} = \frac{3.05C}{B} + 7.9 - \frac{1.8B}{D_q} \qquad (3)$$

where the constant x is defined as

$$x = \frac{E(^4A_{2g} - {}^4T_{1g}) - E(^4A_{2g} - {}^4T_{2g})}{D_q} \qquad (4)$$

From eqn (2)–(4), the crystal field parameters B and C are calculated to be 587 and 3800 cm^{-1}, respectively, which are comparable to those of K_2SiF_6:Mn^{4+} ($10D_q = 23\,900\ cm^{-1}$, $B = 605\ cm^{-1}$, $C = 3806\ cm^{-1}$).[16]

The well-known K_2SiF_6:1% Mn^{4+} red phosphor was prepared for comparison with the Ba_5AlF_{13}:Mn^{4+} phosphor. The excitation spectrum of Ba_5AlF_{13}:Mn^{4+} shifts to lower energy, by about 2400 cm^{-1}, than that of K_2SiF_6:Mn^{4+} as shown in Fig. 5c. This means that the crystal field strength of Mn^{4+} is weaker in the Ba_5AlF_{13} lattice. As reported in ref. 3, the $10D_q$ value depends on the metal–ligand distance according to the relationship $10D_q = K/R^n$, where K represents a constant and the value of n is approximately 5. As calculated in this work and with reference to ref. 3, the Al–F bond distance in the [AlF_6] group is 1.781 Å in Ba_5AlF_{13}, while the Si–F bond distance in the [SiF_6] group is 1.682 Å. Hence, the crystal field strength of Mn^{4+} is weaker in the Ba_5AlF_{13} lattice, which is consistent with the calculated $10D_q$ values above. As a consequence, the excitation spectrum of Ba_5AlF_{13}:Mn^{4+} shifts to lower energy. In addition, the luminescence intensity of the K_2SiF_6:1% Mn^{4+} red phosphor is about three times higher than the phosphor prepared in this work.

Fig. 6 shows the emission spectra and decay curves of the Ba_5AlF_{13}:Mn^{4+} nanoparticles as functions of Mn^{4+} concentration. No difference in spectral features between different Mn^{4+} concentrations is observed in the emission spectra except for the relative intensities of the phonon lines. The emission intensity increases with increasing Mn^{4+} concentration from 0.1 mol% and then reaches the maximum intensity at 0.5 mol%. With a further increase in Mn^{4+} concentration, the emission intensity starts to decrease gradually because of concentration quenching.[17] However, the emission intensity ratio (R) of the integrated ZPL intensity to the integrated ν_6 line intensity depends on the Mn^{4+} concentration as shown in the inset of Fig. 6a. As mentioned above, the intensity of the ZPL depends highly on the local symmetry of the environment surrounding
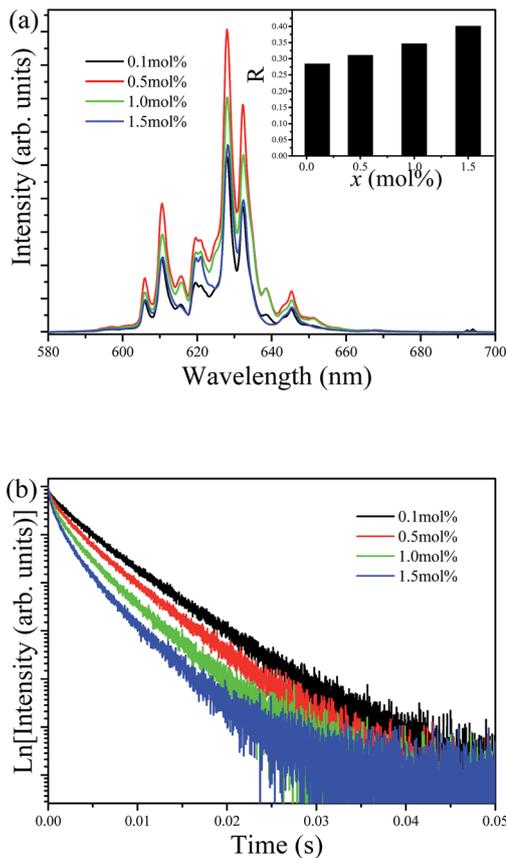

Fig. 6 Emission spectra (a) and decay curves (b) of Ba_5AlF_{13}:Mn^{4+} nanoparticles as functions of Mn^{4+} concentration.

Mn^{4+}. The substitution of the larger Mn^{4+} ion for the smaller Al^{3+} ion gives rise to lattice distortion. Therefore, higher Mn^{4+} concentrations cause more distortion of the [MnF_6] octahedron, thus lowering the crystal field symmetry with larger values of R.

Fig. 6b shows the luminescence decay curves of Ba_5AlF_{13}:Mn^{4+} (0.1–1.5 mol%) nanoparticles obtained by monitoring the 627 nm emission under excitation at 355 nm. The average decay time τ can be calculated by using the following equation.

$$\tau = \frac{\int_0^\infty tI(t)\mathrm{d}t}{\int_0^\infty I(t)\mathrm{d}t} \qquad (5)$$

The decay time decreases with increasing Mn^{4+} concentration and the decay curves gradually deviate from the single exponential. The decay times are estimated to be 8.03, 7.34, 6.07 and 5.13 ms for the Mn^{4+} concentrations of 0.1, 0.5, 1.0 and 1.5 mol%, respectively. Samples with low Mn^{4+} concentrations feature reduced interactions between the Mn^{4+} ions, leading to nearly single exponential decay curves. However, with increasing Mn^{4+} concentration, the distance between the ions shortens; subsequently, energy transfer between the Mn^{4+} ions can occur, which provides an additional decay channel, leading to non-exponential decay curves. A possible explanation for this luminescence quenching is due to the higher nonradiative

energy migration through direct transfer among the Mn^{4+} ions.[18,19]

3.3 Unusual temperature-dependent emission spectra

Fig. 7a shows the emission spectra of Ba_5AlF_{13}:Mn^{4+} (0.5 mol%) as functions of temperature in the temperature region 10–500 K under excitation at 488 nm. As mentioned above, the emission lines are assigned to the spin-forbidden $^2E_g \rightarrow {}^4A_{2g}$ transition of Mn^{4+}, but can gain intensity by the activation of vibronic modes.[20] Some features are worth noting:

(1) The emission spectra show different spectral features at different temperatures. At 10 K, the dominant peaks are those on the low-energy side of the ZPL at 620 nm, while at $T > 100$ K the emission lines become broader and appear not only on the low-energy side but also on the high-energy side, and are known as the Stokes and anti-Stokes emission lines, respectively. At low temperature, the systems are more likely to occupy the vibrational ground state and Stokes emission primarily occurs. However, when the temperature rises, the electrons have enough energy to populate the upper vibration states and relax back to the ground state of $^4A_{2g}$ with anti-Stokes emission.[21]

(2) Based on the temperature dependent emission spectra in Fig. 7a, the total emission intensity as a function of temperature is shown in Fig. 8. The emission intensity increases firstly and then decreases with further increase in temperature. The emission intensity of some previously studied luminescent phosphors consistently decreases with the increase of temperature which is mainly due to the increase of the non-radiative transition probability.[22] However, differently from most oxide lattices, Mn^{4+}-doped fluoride lattices exhibit anti-thermal quenching behavior.[21,23,24] As shown in Fig. 8, the total integrated emission intensity of the $^2E_g \rightarrow {}^4A_{2g}$ transition at 300 K is found to be increased by about 700% compared with the initial intensity at 10 K and then decreased at higher temperatures due to the intense non-radiative transition. It is suggested for Ba_5-AlF_{13}:Mn^{4+} that the increased emission intensity is due to
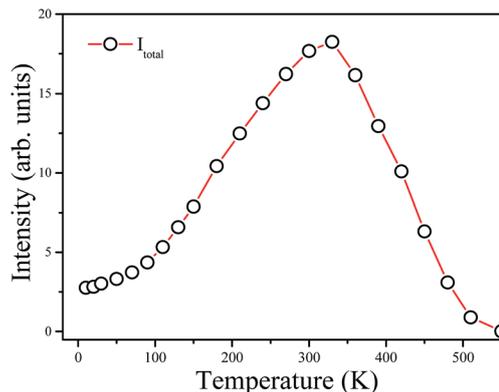

Fig. 8 Integrated intensity of total emission (I_{total}) of Ba_5AlF_{13}:Mn^{4+} as a function of temperature.

expansion of the host lattice and the enhancement of the lattice vibration modes with increasing temperature.[21]

(3) It is observed that all the emission peaks show a tiny red shift and become gradually broader with increasing temperature (Fig. 7b). This is mainly due to the expansion of the unit cell and the enhancement of the vibration modes of the MnF_6^{2-} octahedra in a hot environment.[16]

(4) The shifts of emission peaks and the changes in the relative emission intensity may induce variations of the chromatic coordinates of the phosphor. The dependences of the chromatic coordinates upon the temperature are calculated in Table 1 and shown in Fig. 7c. The x values slightly decrease, while the y values slightly increase, with increasing temperature. The variations in chromatic coordinates are caused by the red-shift of emission bands and the enhancement of anti-Stokes bands.

Fig. 9 shows the decay curves of the 627 nm emission under excitation at 355 nm as functions of temperature. The decays are single exponential at low temperature and become slightly non-exponential at high temperature. The decay times of the ^2E_g state are calculated by using eqn (5). The decay times decrease monotonically from 15.2 ms at 10 K to 1.28 ms at 520 K. The decay times calculated from the temperature-dependent decay curves are shown in Fig. 10a. The temperature dependent decay times of Mn^{4+} can be analyzed by the model for Cr^{3+} suggested by Grinberg.[25] Cr^{3+} is isoelectronic with Mn^{4+} ($3d^3$ configuration). According to this model, an additional relaxation pathway (the spin-allowed $^4T_{2g} \rightarrow {}^4A_{2g}$ transition) occurs with increasing
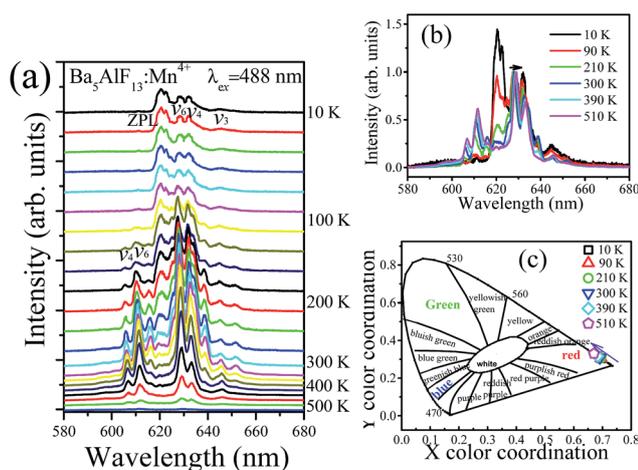

Fig. 7 Temperature dependent emission spectra (a) and normalized emission spectra (b) and CIE chromaticity coordinates (c) of Ba_5-AlF_{13}:Mn^{4+} (0.5 mol%).

Table 1 Calculated CIE values, the ratio R of the anti–Stokes emission intensity to the Stokes emission intensity

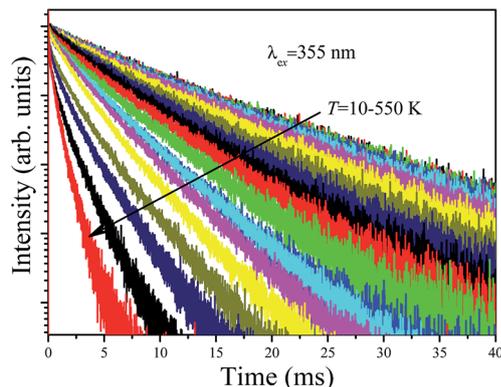| Temperature	x	y
10 K	0.696	0.304
90 K	0.695	0.305
210 K	0.694	0.306
300 K	0.691	0.309
390 K	0.683	0.317
510 K	0.670	0.330

Fig. 9 Temperature dependent decay curves of $Ba_5AlF_{13}:Mn^{4+}$ obtained by monitoring the 627 nm emission under excitation at 355 nm.
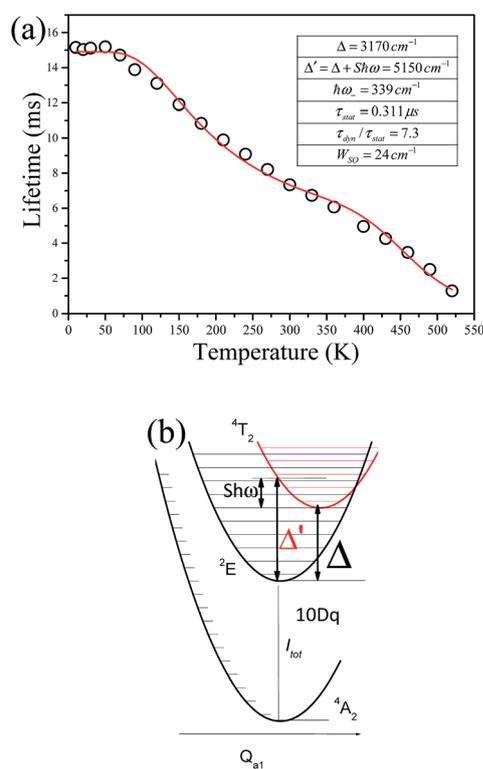

Fig. 10 (a) Decay times of the ^2E state as a function of temperature (10−550 K) for $Ba_5AlF_{13}:Mn^{4+}$ (0.5 mol%). (b) Energy level diagram including the ground state and the lowest excited states without spin–orbit interaction.

temperature and the temperature dependent decay times can be written by the following equation.[26]

$$\tau = \frac{\tau_{stat}\left(1 + \exp\left(-\frac{\hbar\omega_-}{kT}\right) + 3\exp\left(-\frac{\Delta}{kT}\right)\right)}{\left(1 + \frac{\tau_{stat}}{\tau_{dyn}}\exp\left(-\frac{\hbar\omega_-}{kT}\right)\right)\left(\left(\frac{W_{so}}{\Delta'}\right)^2 + 3\exp\left(-\frac{\Delta}{kT}\right)\right)} \quad (6)$$

where Δ' represents the energy difference between the ^2E_g and $^4T_{2g}$ states which can be calculated from the excitation

spectrum. Δ is the energy difference between the minimum energy of the ^2E_g and $^4T_{2g}$ states. $\hbar\omega_-$ is considered as a free parameter for the effective energy of phonons and W_{SO} is an average spin–orbit parameter. $\frac{\tau_{stat}}{\tau_{dyn}}$ is the ratio of the radiative decay times induced by static and dynamic processes. In addition, $\frac{1}{\tau_{dyn}}$ is explicitly independent of temperature.[21]

The temperature dependent decay times are well fitted to eqn (6) and the fit result is shown by the solid red curve in Fig. 10a. The best fit result gives the parameters $\Delta' = 5150\ cm^{-1}$, $\Delta = 3170\ cm^{-1}$, $\hbar\omega = 339\ cm^{-1}$, $W_{SO} = 24\ cm^{-1}$, $\tau_{stat} = 0.311\ \mu s$ and $\frac{\tau_{dyn}}{\tau_{stat}} = 7.3$. The results of the temperature dependent decay times of the ^2E_g state indicate that an additional relaxation pathway (the spin-allowed $^4T_{2g} \rightarrow ^4A_{2g}$ transition) due to the spin–orbit interaction of ^2E_g and $^4T_{2g}$ states occurs with increasing temperature. As calculated, the obtained value of the radiative lifetime τ_{stat} corresponding to $^4T_2 \rightarrow ^4A_2$ is 0.311 μs, which is much shorter than the observed $^2E \rightarrow ^4A_2$ transition. Moreover, the effective spin–orbit coupling energy (24 cm^{-1}) is much smaller than the spin–orbit coupling energy of the spin–orbit interaction Hamiltonian generated by vibronic overlap integrals between the involved states as products of the electronic and vibronic wave functions.[21]

4. Conclusions

$Ba_5AlF_{13}:Mn^{4+}$ nanoparticles were developed by the two-step coprecipitation method. Well-crystallized particles were obtained with sizes ranging from 300 to 500 nm. The phosphors can be effectively excited by near UV – blue light and show bright red emission colors with several sharp lines of emission in the wavelength region 60–660 nm. An intense ZPL emission at 620 nm is observed even at room temperature, which can be attributed to the incorporation of Mn^{4+} ions into highly distorted octahedral lattice sites. The temperature dependent luminescence indicates that the $Ba_5AlF_{13}:Mn^{4+}$ red phosphor shows significant anti-thermal quenching behaviour to increase its emission intensity at 300 K relative to 10 K. In addition, based on the temperature dependent decay curves, a modified dynamic model was constructed, indicating that an additional relaxation pathway (the spin-allowed $^4T_{2g} \rightarrow ^4A_{2g}$ transition) occurs with increasing temperature.

Conflicts of interest

There are no conflicts to declare.

Acknowledgements

References

1 J. C. Boyer, F. Vetrone, L. A. Cuccia and J. A. Capobianco, *J. Am. Chem. Soc.*, 2006, **128**, 7444–7445.

2 M. G. Brika, S. J. Camardello, A. M. Srivastava, N. M. Avram and A. Suchocki, *ECS J. Solid State Sci. Technol.*, 2016, **5**, R3067–R3077.

3 Y. Jin, M. H. Fang, M. Grinberg, S. Mahlik, T. Lesniewski, M. G. Brik, G. Y. Luo, J. G. Lin and R. S. Liu, *ACS Appl. Mater. Interfaces*, 2016, **8**, 11194–11203.

4 L. Huang, Y. W. Zhu, X. J. Zhang, R. Zou, F. J. Pan, J. Wang and M. M. Wu, *Chem. Mater.*, 2016, **28**, 1495–1502.

5 H. M. Zhu, C. C. Lin, W. Q. Luo, S. T. Shu, Z. G. Liu, Y. S. Liu, J. T. Kong, E. Ma, Y. G. Cao, R. S. Liu and X. Y. Chen, *Nat. Commun.*, 2014, **5**, 4312–4321.

6 M. H. Fang, H. D. Nguyen, C. C. Lin and R. S. Liu, *J. Mater. Chem. C*, 2015, **3**, 7277–7280.

7 L. L. Wei, C. C. Lin, Y. Y. Wang, M. H. Fang, H. Jiao and R. S. Liu, *ACS Appl. Mater. Interfaces*, 2015, **7**, 10656–10659.

8 T. Han, T. C. Lang, J. Wang, M. J. Tu and L. L. Peng, *RSC Adv.*, 2015, **5**, 100054–100059.

9 H. Bode, H. Jenssen and F. Bandte, *Angew. Chem.*, 1953, **65**, 304.

10 C. Martineau, M. Allix, M. R. Suchomel, F. Porcher, F. Vivet, C. Legein, M. Body, D. Massiot, F. Taulelle and F. Fayon, *Dalton Trans.*, 2016, **45**, 15565–15574.

11 R. D. Shannon, *Acta Crystallogr., Sect. A: Cryst. Phys., Diffr., Theor. Gen. Crystallogr.*, 1976, **32**, 751.

12 B. Henderson and G. F. Imbusch, *Optical Spectroscopy of Inorganic Solids*, Oxford University Press, 1989.

13 A. Lempicki, L. Andrews, S. J. Nettel, B. C. McCollum and E. I. Solomon, *Phys. Rev. Lett.*, 1980, **44**, 1234–1236.

14 D. Sekiguchi and S. Adachi, *ECS J. Solid State Sci. Technol.*, 2014, **3**, R60–R64.

15 Y. C. Chang, C. H. Liang, S. A. Yan and Y. S. Chang, *J. Phys. Chem. C*, 2010, **114**, 3645–3652.

16 L. L. Wei, C. C. Lin, M. H. Fang, M. G. Brik, S. F. Hu, H. Jiao and R. S. Liu, *J. Mater. Chem. C*, 2015, **3**, 1655–1660.

17 M. Y. Peng, X. W. Yin, P. A. Tanner, C. Q. Liang, P. F. Li, Q. Y. Zhang and J. R. Qiu, *J. Am. Chem. Soc.*, 2013, **96**, 2870–2876.

18 Y. H. Jin, Y. R. Fu, Y. H. Hu, L. Chen, H. Y. Wu, G. F. Ju, M. He and T. Wang, *Powder Technol.*, 2016, **292**, 74–79.

19 R. P. Cao, Y. J. Ye, Q. Y. Peng, G. T. Zheng, H. Ao, J. W. Fu, Y. M. Guo and B. Guo, *Dyes Pigm.*, 2017, **146**, 14–19.

20 D. Sekiguchi, J. Nara and S. Adachi, *J. Appl. Phys.*, 2013, **113**, 183516–183522.

21 W. L. Wu, M. H. Fang, W. L. Zhou, T. Lesniewski, S. Mahlik, M. Grinberg, M. G. Brik, H. S. Sheu, B. M. Cheng, J. Wang and R. S. Liu, *Chem. Mater.*, 2017, **29**, 935–939.

22 B. Wang, H. Lin, J. Xu, H. Chen and Y. S. Wang, *ACS Appl. Mater. Interfaces*, 2014, **6**, 22905–22913.

23 L. Y. Wang, E. H. Song, Y. Y. Zhou, T. T. Deng, S. Ye and Q. Y. Zhang, *J. Mater. Chem. C*, 2017, **5**, 7253–7261.

24 T. T. Deng, E. H. Song, J. Sun, L. Y. Wang, Y. Deng, S. Ye, J. Wang and Q. Y. Zhang, *J. Mater. Chem. C*, 2017, **5**, 2910–2918.

25 M. Grinberg, *Opt. Mater.*, 2002, **19**, 37–45.

26 Z. Pan, Y. Y. Lu and F. Liu, *Nat. Mater.*, 2012, **11**, 58–63.